Epithelial folding of alveolar cells derived from human induced pluripotent stem cells on artificial basement membrane

Elrade Rofaani, Yong He, Juan Peng, Yong Chen

Epithelial folding of alveolar cells derived from human induced pluripotent stem cells on artificial basement membrane

Elrade Rofaani[1,2], Yong He[1], Juan Peng[1], and Yong Chen[1*]*

[1] PASTEUR, Département de chimie, École normale supérieure, PSL University, Sorbonne Université, CNRS, 75005 Paris, France

[2] National Research and Innovation Agency, Jakarta, 10340, Indonesia

Corresponding Author

**Yong CHEN*: yong.chen@ens.psl.eu; **Juan PENG*: juan.wang@ens.psl.eu

KEYWORDS: hiPSC, epithelium, basement membrane, folding

ABSTRACT

Epithelial folding depends on mechanical properties of both epithelial cells and underlying basement membrane (BM). While folding is essential for tissue morphogenesis and functions, it is difficult to recapitulate features of a growing epithelial monolayer for in vitro modeling due to lack of in vivo like BM. Herein, we report a method to overcome this difficulty by culturing on an artificial basement membrane (ABM) the primordial lung progenitors (PLPs) from human induced pluripotent stem cells (hiPSCs). The ABM was achieved by self-assembling collagen IV and laminin, the two principal natural BM proteins, in the pores of a monolayer of crosslinked gelatin nanofibers deposited on a honeycomb micro-frame. The hiPSC-PLPs were seeded on the ABM for alveolar differentiation under submerged and air-liquid interface culture conditions. As results, the forces generated by the growing epithelial monolayer led to a geometry-dependent folding. Analysis of strain distribution in a clamped membrane provided instrumental insights into some of the observed phenomena. Moreover, the forces generated by the growing epithelial layer led to a high-level expression of surfactant protein C and a high percentage of aquaporin 5 positive cells compared with the results obtained with a nanofiber-covered bulk substrate. Thus, this work demonstrated the importance of recapitulating natural BM for advanced epithelial modeling.

1. INTRODUCTION

Epithelial cell layers are self-organized on the outer surfaces of organs and blood vessels as well as the inner surfaces of many internal organs of our body. They are thin, continuous, and often folded to form various morphologies [1,2]. To understand the mechanism that underlies epithelial formation, advanced in vitro models are needed. However, the previous studies relied mostly on culture dishes, flasks, multiwell plates, and transwell membranes which are stiff and cannot be bent with the growing epithelial cell layers [3]. A lot of efforts have been devoted to the development of new culture substrates, including electrospun nanofibers, hydrogels, pillar arrays, and 3D printing scaffolds [4]. These approaches unambiguously evidenced the importance of the mechanical property and surface morphology of the culture substrate but yet they were not able to recapitulate the essential features due to the lack of an in vivo like basement membrane (BM) on which the epithelial cells grow and are self-organized. While the BM is an ultrathin layer made of specific extracellular matrix proteins (mainly collagen IV and laminin), it is semipermeable and acts as a platform for complex signaling to the attached epithelial cells [5]. In vivo studies have shown that the BM follows closely the folding of the epithelial cell layer it supports and that it can also be regulated by the cells through protein degradation and protein secretion [6,7]. It is therefore important to consider the epithelial cells and the underlying BM as an assembly in order to develop new in vitro models [8,9]. Interestingly, the formation of organoids begins with a cell cluster embedment in gel BM proteins. With the increase of the organoid size, a BM-like shell emerges and budding structures appear due to epithelial self-organization [10,11]. This is intriguing for the development of sheet-like tissue models which are often needed for easy analysis and assessment of the epithelium interfaces.

Alveolar epithelium is particular interesting for understanding lung diseases and addressing many fundamental issues [12]. The alveolar epithelium is mainly composed of alveolar type I (AT1) and type II (AT2) cells. While AT1 cells are large squamous cells covering 95% of the alveolar surfaces, AT2 cells are cuboidal cells secreting pulmonary surfactant and serving as alveolar stem cells. During alveolar homeostasis and post-injury repair, AT2 cells can be differentiated into AT1 cells [13]. Since the alveolar epithelium is constantly subjected to cyclic deformation, the differentiation of the AT2 cells into AT1 cells should be deformation dependence but how this is correlated to the injury and repair of the epithelium is unclear. Immortalized cell lines such as A549 [14] and NCI-H441 [15] were commonly used in alveolar modeling but they are both AT2-like and lack phenotype heterogeneity due to their cancer origins. Alternatively, alveolar cells derived from human

induced pluripotent stem cells (hiPSCs) can be both AT1 and AT2 cells and open the possibility to develop patient-specific models [16-19]. While hiPSCs are capable of self-renewing and differentiating into either lung progenitor cells or matured alveolar cells, it is important to optimize the differentiation protocols and conditions in order to achieve a more realistic modeling for physiological or pathological studies. In general, hiPSCs were firstly induced into definitive endoderm (DE) and anterior foregut endoderm (AFE) under conventional culture conditions. Then, the cells were differentiated into alveolar cells via alveolar progenitors by using different strategies [16-23]. One of the main strategies is to plate cells on a transwell membrane for submerged and air-liquid interface (ALI) culture [17]. Obviously, plating primordial lung progenitors (PLPs), alveolar progenitor cells (APC) or mature alveolar cells may have different outputs in terms of cell composition and epithelial organization. An early-stage plating would rely more on rapid proliferation and strong self-organization of the differentiating progenitor cells, while a later stage replating would lead to a limited cell proliferation with a gentle tissue organization. In this regard, the stiffness of the membrane can significantly influence the performance of the cell organization. Transwell and microfabricated membranes with synthetic materials and surface coating techniques could be used but they should not be appropriate for alveolar folding studies [16,24,25].

Substrate stiffness has a profound influence not only on the adhesion, proliferation, and differentiation of the alveolar cells but also on the organization and folding of alveolar cell layers. Previously, we developed a method to reconstitute BM by self-assembling collagen IV and laminin in the pores of a monolayer of crosslinked gelatin nanofibers [26]. Such an artificial basement membrane (ABM) is in vivo like in terms of morphology, mechanic properties, and bioactivity. In this work, we focus on the folding of epithelial-generated forces and their impact on cellular properties by plating early-stage lung progenitor cells on the ABM. We hypothesize that the progenitor proliferation generated forces are large enough to deform and fold the underlying BM and that the contractile force promotes both alveolar differentiation and alveolar maturation. We will firstly generate PLPs from hiPSCs in the dish. Then, we plate the hiPSC-PLPs on the ABM to observe the proliferation-induced epithelial formation and folding. Finally, we analyze the expression of the matured alveolar cells and the percentage of AT1 cells. The results will be compared with two other types of substrates, i.e., glass and nanofiber-covered glass (NFS). In addition, an approximative analytical model will be used to calculate the geometry-dependent strain distribution.

2. EXPERIMENTAL SECTION

2.1. Fabrication and characterization of the ABM

The reconstituted basement membrane consists of a thin layer of collagen IV and laminin self-assembled with a monolayer of crosslinked gelatin nanofibers as backbone and a lithography-pattern honeycomb microframe for nanofiber handling (Figure 1A, S1). Briefly, a honeycomb structure of 400-μm hole size and 50-μm linewidth and thickness were defined in a SU-8 photoresist (Microchem, France) by photolithography. A second layer of photolithography was performed to add a ring of thickness 100 μm and diameters 9 and 13 mm. This pattern was sequentially replicated into polydimethylsiloxane (PDMS, Eleco-EFD, France) by casting and polyethylene glycol diacrylate (PEGDA) by vacuum-assisted UV-curing. Afterward, the positive tone replica (frame) was coated by 10 nm Au for electrospinning of gelatin nanofibers. 10 wt% gelatin powders (#61890, Sigma-Aldrich, France) were dissolved in a mixed solution of acetic acid, ethyl acetate (#270989, Sigma-Aldrich, France), and distilled water at a volume ratio of 21:14:10. The nanofibers were deposited at a distance of 10 cm and voltage 11 kV for 3 or 5 min, controlled with a high voltage supply (Heinzinger, Germany), a syringe pump (#78-9100B, Kd Scientific, USA) at a feeding rate of 0.2 mL/h. After electrospinning, gelatin nanofibers were dried in a desiccator overnight and cross-linked in a 0.2 M mixture of 1-ethyl-3-(3-dimethylaminopropyl) carbodiimide hydrochloride (EDC) (#6383, Sigma-Aldrich, France) and N-hydroxysuccinimide (NHS) (#130672, Sigma-Aldrich, France) in ethanol for 4 h. After crosslinking, a monolayer of gelatin nanofibers was obtained. To eliminate remaining toxic chemicals, samples were rinsed in 99.5% ethanol three times, dried in a vacuum overnight, and finally submerged in sterilized water overnight.

To form ABM, a 50 μL solution composed of 0.1% (w/v) collagen IV (#C7521, Sigma-Aldrich, France) in water containing 0.1 M acetic acid and 2% (v/v) laminin (#L2020, Sigma-Aldrich, France) was pipetted on the crosslinked nanofibers. After dehydration at 37°C for 3–5 h, a continuous film of collagen IV-laminin mixture was obtained. For comparison, gelatin nanofibers were also deposited and chemically crosslinked on a gold-coated 13-mm diameter cover glass, referred as nanofibers substrate or NFS, in a similar way as described above.

Finally, the fabricated monolayer of nanofibers and ABM were characterized by electron scanning microscopy for the determination of nanofiber diameters, the porosity of the nanofiber monolayer and the thickness of the ABM. Measurements of the membrane deflection and the transmembrane flowrate were also performed as a function of pressure for the estimation of the ABM stiffness and permeability, in a similar way as described in [23].

2.2. Generation of alveolar epithelial cells

hiPSCs (episomal line, Life Technologies) were cultured and maintained in complete Essential 8 Flex medium (#A2858501, Gibco) with a 1:100 diluted vitronectin (#A27940, Life Technologies)-coated culture dish and incubated at 37˚C with 5% CO_2 condition. The medium was changed every two days until cells grew to 70–80% confluence. Cells were harvested with a solution of DPBS (Dulbecco's Phosphate Buffered Saline, #14190-094, Gibco) with 0.5 mM EDTA (#15575-038, Life Technologies).

hiPSCs were differentiated into finite lung progenitor cells and then matured alveolar epithelial cells [22-24] by using different types of substrates, all coated with (1%) Geltrex. Overall, hiPSCs were derived sequentially to (i) definitive endoderm (DE) (6 days), (ii) anterior foregut endoderm (AFE) patterning (2 days), (iii) AFE ventralization into a bipotential PLPs (7 days), (iv) development of PLPs into APCs (6-10 days), and final (v) mature alveolar epithelial cells (AECs) (about 17 days) (Figure 1B).

DE induction: Prior to induction, hiPSCs were cultured in a vitronectin-coated dish until reaching 50% confluence. The induction medium of serum-free RPMI1640 (#21875034, Gibco) containing 1% glutamine, 1% penicillin-streptomycin (pens-strep, #15140122, Gibco) and 1% non-essential amino acid (NEAA) or B-27 (#17504-044, Gibco), and 0.1% ascorbic acid (#A4403, Sigma-Aldrich), was prepared with high concentration of Activin A (100 ng/mL) (#78001.1, STEMCELL Technologies) and 1 μM CHIR-99021 (#SML1046, Sigma-Aldrich). The cells were induced in this medium for 6 days to generate DE or to undergo a gastrulation process. The medium was changed every two days.

AFE patterning: From day 6 to day 8, cells were treated with serum-free IMDM medium (#12440-053, Gibco) containing 1% glutamax, 1% pens-strep, 1% B-27 and 0.1% ascorbic acid, as a serum-free IMDM medium, then supplemented with 10 μM SB-431452 (#HB3555, Hellobio) and 1.5 μM dorsomorphin or DSM (#P5499, Sigma-Aldrich).

PLPs generation: From day 8 to day 15, cells were cultured in a serum-free IMDM medium containing 3 μM CHIR-99021, growth factor of 10 ng/mL KGF or FGF-7 (#251-KG, R&D System), 10 ng/mL BMP4 (#78211, STEMCELL Technologies) and 0.0625 μM retinoic acid or RA (#R2625, Sigma-Aldrich).

APCs derivation: On day 15, PLPs were digested with tryplE (#12605-010, Life Technologies) for 5 min and seeded in diluted 1% Geltrex- (#A1413302, Life Technologies) coated ABM, NFS, and glass. The cells were resuspended in a serum-free IMDM medium containing 3 μM CHIR-99021 and a growth factor for epithelium proliferation, 10 ng/mL KGF. The medium was changed every two days until day 21.

APCs maturation: From day 22 to day 39, APCs were cultured in a serum-free IMDM medium containing 3 µM CHIR-99021, 10 ng/mL KGF, and a cocktail molecule, composed of 0.1 mM 8-bromo-cAMP (#D0627, Sigma-Aldrich), 25 ng/mL dexamethasone (#4902, Sigma-Aldrich) and 0.1 mM isobutyl methylxanthine (iBMX, #I5879, Sigma-Aldrich) which are referred to as DCI. The ABM device with cells was mounted in a homemade transwell-like support (Fig. S2) with cells in the apical compartment and the assembly was placed in a 6 well plate (#734-2323, VWR) for culture under ALI conditions (Figure 1C and S1). After one day of culture, the medium in the apical compartment was gently removed and washed by DPBS for three times, leaving the apical surface of the cells exposed to air (an atmosphere of 5% CO_2 at 37°C). Afterward, the culture was continued and the medium in the low compartment was changed every two days.

2.3. Immunofluorescence microscopy

Cells were rinsed with DPBS and fixed with 4% paraformaldehyde (#P6148, Sigma-Aldrich) for 15 min. Samples were permeabilized with 0.5% Triton X-100 (#HFH10, Life Technologies) for 20 min and saturated in a blocking solution (3% bovine serum albumin (#A9056, Sigma-Aldrich), 0.1% Tween 20 (#P1379, Sigma-Aldrich), and 0.1% sodium azide (w/v) in DPBS) for 2 h at room temperature. The samples were further incubated with primary antibodies at 4 °C overnight, followed by the incubation with secondary antibodies in the blocking solution for 2 h and subsequent nuclei staining in PBS containing 1 µg/mL DAPI for 15 min at room temperature. The following primary antibodies were used for immunostaining: anti-NKX2.1 (1:100, #MA5-13961), anti-ZO-1 (1:100, #40-2200), anti-SFTPC (1:25, #PA5-71680), anti-ACE2 (1:1000, #MA5-31394) and anti-TMPRSS2 (1:50, #PA5-14264) from Invitrogen, anti-AQP5 (1:100, #SC-9890) from Santa-Cruz. All Alexa Fluor conjugated secondary antibodies are from Invitrogen, and the corresponding secondary antibodies were diluted in 1:250. All samples were observed with an LSM Zeiss 710 confocal microscope (Zeiss, France). Images were collected as TIF files and analysed with the software ImageJ.

2.4. Statistical analysis

All group data are expressed as mean ± SEM. The comparisons between groups were performed using Student t-test. Differences between groups were considered significant when $P < 0.05$ ($^{*}P < 0.05$; $^{**}P < 0.01$; $^{***}P < 0.001$).

2.5. Numerical simulation

The epithelial folding was interpreted in terms of inhomogeneous strain distribution in a deflected plate clamped with a hexagonal frame. For the sake of simplicity, an elastic plate under uniform pressure can be considered. Based on von Karman plate theory, the radial (e_r) and tangential (e_t) strains of a circular plate of radius *a* can be calculated by using [27],

$$e_r - e_0 = \frac{du}{dr} + \frac{1}{2}\left(\frac{dw}{dr}\right)^2 \quad (1)$$

$$e_t - e_0 = \frac{u}{r} \quad (2)$$

where e_0 is the initial strain, *u* and *w* are the radial and transverse displacement of the plate, respectively, *r* the radial distance from the center of the plate. After some algebra, the following solution is obtained [30].

$$\mathrm{u} = \frac{5-3\upsilon}{6}\left(\frac{w_0^2}{a^2}\right)\mathrm{r} + \frac{-3+\upsilon}{1}\left(\frac{w_0^2}{a^4}\right)r^3 + \frac{10-2\upsilon}{3}\left(\frac{w_0^2}{a^6}\right)r^5 + \frac{-7+\upsilon}{6}\left(\frac{w_0^2}{a^8}\right)r^7 \quad (3)$$

where υ is the Poisson's ratio, w_0 the displacement at the center of the plate, which can be calculated by substituting equ. (3) and $w = w_0(1 - r^2/a^2)^2$ into equ. (1) and (2),

$$\frac{Pa^4}{64D} = \left[1 + \frac{3}{4}\left(\frac{a}{h}\right)^2(1-\upsilon^2)\frac{\sigma_0}{E}\right]w_0 + (0.4118 + 0.25\upsilon - 0.16088\upsilon^2)\frac{w_0^3}{h^2} \quad (4)$$

where *D* is the bending modulus $D = E\hbar^3/12(1-\upsilon^2)$, P the pressure, *E* Young's modulus, σ_0 the residual surface stress, and *h* thickness of the membrane. Thus, *E* and σ_0 can be deduced by fitting experimental data of w_0 as a function of P. Consequently, the distribution of radial and tangential strains in the place can be derived. Finally, numerical simulations were performed by solving the above equations.

3. RESULTS

3.1. Properties of the ABM

The fabricated ABMs have a backbone of crosslinked gelatin nanofibers of the average thickness of ~200 nm and average porosity of ~30 %, both determined by analyzing SEM images (Figure 1A). The hexagonal structure is 500 μm in pitch and 50 μm in thickness and width. After self-assembling, the BM proteins, the pores of the nanofibers were filled but the thickness of the membrane was unchanged when a solution of low protein concentration was used for dropping and dehydration, as detailed in 2.1. The contact angle of the ABM is 38°, 50°, and 54° with distilled water, PBS, and culture medium, respectively [28]. The stiffness of the ABM was deduced by using equ. (4) after measuring the deflection of the ABM in one

hexagon of the frame as a function of applied pressure in a similar way as described in [23,29]. By data fitting, the effective Young's modulus of PDMS and PDMS-ABM assembly could be deduced. Then, assuming that 25% stiffness of the assembly was due to ABM, we deduced an effective Young's modulus of the ABM, E_s = 4.9 MPa, which was compared to that of the nanofiber backbone. The permeability of the ABM was deduced by measuring the flow rate of DI water crossing an ABM as a function of applied pressure, which is 860 nm². The strength of cell attachment on the ABM was compared with that on NFS and glass by spinning the cell samples, showing remarkable morphology change or detachment of the cells on NFS or glass substrate but cells stayed wells after shaking at 800 rpm for 10 min and spinning at 2000 rpm for 10 s [30]. Finally, cell culture was performed under a transwell-like culture where the apical compartment with cells was filled with buffer and the basal compartment was filled with the medium so that the nutrient for cells came from the basal compartment by diffusion, showing the feasibility of diffusion culture and proliferation cross the ABM.

3.2. Numerical results of strain distribution

Let us now consider a 200 nm thick elastic membrane clamped with a 500 μm size hexagonal frame, Young's modulus of E_s = 4.9 MPa, a Poisson's ratio of υ =0.5, and a deflection of 100 μm in the membrane center. For the zeroth order of approximation, we also assume that the radial distribution of the strains depends only on the distance to the edge of the frame. Then, we used equ. (1)-(3) to calculate the distribution of the radial and tangential strains along the direction to vertices and equal sides (Figure S3A and S3B) and plotted the maximum of radial strain (red) and the minimum of tangential strain (blue) (Figure S3C). Here, the linewidth of the plots is proportional to the amplitude of the strain. The grey line represents the periphery of the hexagonal frame. Clearly, the maximum radial and the minimum tangential strain appear at a distance of ~0.6 r/a and ~0.85 r/a, respectively. In addition, the hexagonal geometry of the frame gives rise to an angle-dependent strain distribution, leading to a rotational symmetry of order 6 and consequently a potential folding of the same order.

3.3. Deformation and folding of lung progenitors on ABM

The stepwise differentiation started by endoderm germ lineage specification with hiPSC monolayer colonies with 50% confluency and a culture medium with Activin A and CHIR-99021 over 6 days (Figure 1B, S4). On days 7 and 8, the cells were patterned into AFE by

inhibiting the bone morphogenic protein (BMP) and TGF-β signaling pathways. Then, the cells became PLPs to form epithelial- and cyst-like features from day 9 to day 15. On day 15, PLPs were replated on different substrates for epithelial formation.

The phase-contrast images in Figure S5 show the distributions of the progenitors' cells one and six days after replating on different substrates (days 16 and 21), respectively. Apparently, the cells aggregated one day after replating before spreading. Compared to nanofiber-conditioned substrates, significantly fewer cells remained on the glass. On day 21, the cells were stained with primary antibodies for ventral marker NKX2.1 (homeodomain-containing transcription factor) [31] and apical tight junction (TJ) marker ZO-1 (Zonula occludens-1) [32]. Figure 2 shows confocal immunofluorescence images of the cells on ABM in one of the honeycomb compartments, revealing a striking effect of epithelial folding. The top-down cross-sectional view images illustrate the folding features in the range of observation (Figure 2A). Clearly, the folding was more important in the proximity of the edge. Although the folding did not follow the geometry of the boundaries, the number of folds was not far from the number of the hexagonal compartment. Moreover, taking into account the parts out of the scope, a folding amplitude in the order of 100 µm could be estimated. Figure 2B displays the top view of a 3D construction of cell images with ZO-1 staining, showing junctional remodeling and appearance of both moat-like invaginations and evagination, similar to villi and crypts-like features in intestinal mucosa/epithelium [33]. Figure 2C shows cross-sectional views at several XZ planes of the 3D image, clarifying both wavy features and ZO-1 protein location of the epithelial cells. Finally, Figure 2D shows expression levels of NKX2.1 and ZO-1 proteins for a given cross-section, indicating an inhomogeneity and presumably an inhomogeneity in cell types or cell functions depending on the location of the cells and. These results suggest that the folding is accompanied by the increase of the cell number due to the high proliferation ratio and low stiffness of the ABM. Roughly speaking by considering a dome-like deflection of 100 µm, a 25% of area increase can be estimated. Taking into account lateral shrinking of the cells, an increase in cell number of higher percentages could be expected. Of note, the progenitor layers remained flat on glass and NFS since both substrates could not be deflected.

Figure 3 shows a further comparison in regard to distribution and morphometry of the APCs on three different types of substrate. Immunofluorescence images of two ROIs were displayed to show different expression levels (green and red) and different cell organizations (blue) for each type of substrates. Comparatively, the cells on glass and NFS were more

expanded than that on ABM, however, the latter has a higher cell density in a unit area (Figure 3A, C). Moreover, we have observed uneven distribution of cells on the glass, revealed by two quite different cell densities shown in ROI1 and 2. Although the cell arrangement on the NFS seemed more homogeneous (ROI3), small cysts could be formed and sporadically interspersed in the cell layer (ROI4), identified by ZO1- indicated single lumen formation (yellow circle). Remarkably, cells on ABM maintained a monolayer and planar-polarized structure, with dynamic junctional remodeling. On the one hand, a symmetrical pattern with radial ZO-1 segment presents a high-order vertex in a rosette, giving rise to elongated wedge-shaped cells. This kind of apical constriction forced the epithelium into a concave apical surface with an enlarged basal area (ROI5) (yellow circle). On the other hand, the apical surface was comparatively increased for cells in the bulging area (ROI6). They are transient and unstable structures. If the apical constriction determined the location of the tissue deformation, the mechanic force of cell proliferation would amplify the tissue deflects. Consequently, our results show that the alveolar epilayer was folded due to cell expansion in the limited area of the honeycomb compartment. Figure 3B showed schematic diagrams of cell reorganization (top views) and cell layer morphometry (section views) on ABM.

3.4. Maturation of alveolar epithelial cells

The ABM with APCs was mounted in a homemade Boyden chamber on day 22 for maturation under ALI culture conditions. The cells on NFS remained under submerged culture conditions for another 17 days. In this stage, the glass sample was no more considered because of the easy cell detachment. Figure 4 shows immunofluorescence images of matured alveolar cells on the ABM labelled on day 39 by AT2-associated marker surfactant protein C (SFTPC) and AT1 cell-associated marker aquaporin 5 (AQP5), providing a general view of cell distribution and deflection of the epithelium. Statically, the epithelium formed in most of the honeycomb compartment was deflected but the degree of their deflection varies and folding is location dependent. Here, a slightly deformed concave epithelium was chosen for analyses. In the bottom area of the concave, the cells were mostly AQP5+ cells, while the SFTPC+ cells were more likely distributed on the side area of the concave. Clearly, SFTPC proteins were mainly produced in the apical domain of the cells. From the top view of the images, one can see that more SFTPC+ cells were concentrated in the area close to the circle of the guiding eye as indicated. This could be due to the non-uniform distribution of radial and tangential strain of the underlying ABM. Nevertheless, the distribution of AQP5+ cells was more homogenous.

More detailed analyses were performed for comparison between ABM- and NFS-supported alveolar epithelial cells. Figure 5A shows the merged immunofluorescence images of the cells on the two types of substrates. Again, a remarkable folding was observed with the ABM sample, indicating that the deformation and folding effect remained during the entire maturation stage (Figure 5B). As can be seen in Figure 5C, the cells on NFS mostly expressed SFTPC proteins on the bottom side of the cell layer and only a limited number of cells were AQP5+. More AT1 cells were could be generated on ABM than that on NFS, which confirms the advantage of using ABM. This can also be evidenced by comparing the fluorescence intensity of both SFTPC and AQP5 proteins of the cells (Figure 5D and 5E). Our numerical analysis also showed a much-increased percentage of AQP5+ cells on ABM compared to that on NFS (33% against 9%), but the number of SFTPC+ cells on both types of substrates remained significantly higher than that of in vivo [34,35], similar to that of previous in vitro models [20, 22] (Figure 5F). Globally, twice of SFTPC+ and AQP5+ cells were observed on ABM than on NFS (Figure 5F), indicating more cells reached a mature stage due to a low stiffness of the substrate [36]. Finally, the cell density on the ABM was about twice that before maturation (Figure 5G) but the cell height remained almost the same as before (Figure 5H). Compared to the NFS, the alveolar cells on the ABM have a much higher density and a much-elongated cell shape due to the improved cell-matrix adhesion and cell-cell coupling as well as the improved cell proliferation and survival rate.

3.5. Alveolar expression of ACE2 and TMPRSS2

Expression of ACE2 and TMPRSS2 was also examined by immunofluorescence imaging. ACE2 (angiotensin-converting enzyme 2) is an enzyme attached to the membrane of cells and capable to convert angiotensin II to angiotensin 1-7 that counter regulate pro- and anti-inflammatory pathways of cells. It can therefore be considered as a potential diagnostic and prognostic biomarker for chronic inflammatory lung diseases [39,40]. Figure 6 shows the immunofluorescence images of matured alveolar cells on NFS and ABM, revealing that more cells expressed ACE2 on ABM than on NFS and that the ACE2 expression level of the cells on the two types of substrates are comparable. Moreover, the ACE2 expression of the cells on ABM was dispersed (ABM-D as indicated by white arrow) or clustered (ABM-C), while only clustered expression of ACE2 was observed with the cells on NFS. The high percentage of ACE2+ cells on the ABM would suggest a high degree of cell maturation probably not only involving the AT2 cells. Finally, the expression of TMPRSS2 (transmembrane protease, serine 2) of the cells was also examined. As shown in Figure 6D, the TMPRSS2 expression of

the cells was more homogenous, suggesting that the expressions of the two proteins were not correlated.

4. DISCUSSION

Here, we present an in vitro model to study the effect of epithelial folding by differentiating cells on the ABM. Such an ABM is an ultrathin dense and sheet-like ECM, self-assembled in the porous area of a monolayer of crosslinked gelatin nanofibers deposited on a patterned honeycomb micro-frame. The properties of the ABM, including the surface morphology, stiffness, permeability, wetting, and cell adhesion behaviors, were evaluated to demonstrate the suitability of the device for cell culture, epithelial formation, and studies of the folding effects. hiPSC-PLPs were used to generate folded epithelium due to cell proliferation and pliable characteristics of the ABM. Besides, a simple calculation was introduced to explain the observed folding effect. Compared to the previous in vitro studies which relied mostly on cell growth on a patterned surface [37-39], the present approach is more generic and applicable with various physiological and pathological conditions.

Gelatin was chosen to produce electrospun nanofibers based on our previous studies on hiPSC culture and differentiation [40-43]. Gelatin is a degraded form of collagen which is the most abundant protein in our body. We have shown that hiPSCs cannot propagate on flat gelatin layers due to insufficient cell attachment but they can be expanded over more than 10 generations on a surface with nanofibrous morphology [44]. Moreover, a suspended monolayer of crosslinked gelatin nanofibers can be easily used as the backbone for the self-assembling of BM proteins. Of note, gelatin nanofibers alone might be digested by mature epithelial or endothelial cells, but they become more stable after BM protein self-assembling and even more stable when used for coculture of epithelial and endothelial cell layers [23,30]. Finally, gelatin is a hydrogel with relatively low stiffness, while the effective Young's modulus of a monolayer of nanofibers may even be much lower than that of bulk as determined in 3.1. Based on the theory of cellular solids [45], the effective Young's modulus of the gelatin nanofiber structure can also be calculated analytically. Considering a hexagonal lattice of segment length of l, thickness of $2a$, and material Young's module of E_s, the in-plane and out-of-plane Young's moduli of the structure are given by $E=\frac{4}{\sqrt{3}}E_s(\frac{2a}{l})^3$ and $E=\frac{2}{\sqrt{3}}E_s(\frac{2a}{l})$, respectively. Assuming a ratio of thickness to segment length of 0.1 and a material Young's modulus of 4.9 MPa, we obtain an effective in-plane and out-of-plane Young's modulus of 3.12 kPa and 156 kPa respectively. After self-assembling BM proteins,

the in-plan and out-of-plan Young's moduli might be in the same order of its backbone and comparable to that of human lung tissues [8].

In the present work, only two principal proteins of the BM (collagen IV and laminin) were used for the preparation of the ABM but adding other BM components such as entactin/nidogen and perlecan should be beneficial for the quality improvement of the ABM since they are potential linkers of collagen IV and laminin networks [5,6]. As an epithelial culture platform, the cell adhesion relies on the interaction between BM proteins and integrins through the hemidesmosome complex [46,47], while significant crosstalk exists between integrins and cadherins [47], the two responsible for mechanotransduction during development and tissue morphogenesis [48]. Obviously, growing epithelial cells can degrade, secrete, and deposit BM proteins, making them an indissociable assembly. We assume that ABM is an important enabling factor for the early setting of epithelial tissue layers. A systematic study on such a naturally occurred complexity would be interesting.

Coming back to the folding effect, the interplay between the growing epithelial cells and the underlying BM results in the morphology of the epithelium. While the epithelial generated forces are due to the increase in cell number, the integrity of the epithelium depends on the coupling between cells and BM proteins as well as the stiffness and permeability of the BM [49-54]. If the substrate is stiff or the cell-BM adhesion is weak, the proliferation-induced excess cells could be extruded and cell growth could be stopped. Otherwise, the excess cells lead to the accumulation of actin and myosin-based contraction forces which may deflect or fold the substrate [55,56]. In our case, both hiPSC-PLPs and hiPSC-APCs are capable to expand during their differentiation processes and both are able to deform the underlying ABM. In addition, the ABM is ultrathin and highly permeable to nutrients and metabolites which favorite the monolayer cell organization and the hemostasis of the system no matter the epithelium is folded or not. Obviously, this is not possible with a stiff substrate or conventional membranes.

Epithelial folding is a common effect or a general strategy of tissue formation when generating spatial structure in the three-dimensional space as observed in the lung, kidney, intestines, and stomach. These organs exhibit a variety of folded multicellular structures in favoring the exchange of nutrients and metabolites. Typically, these structures are periodic with pitch size in the order of 100 µm, which is comparable to the side length of the honeycomb micro-frame of the ABM device and the folding feature we observed (Fig.2). From a physical point of view, folding is expected in a growing constrained system due to buckling instability [57]. Since neither ABM nor epithelial cell layer is simply elastic, the

numerical results of Fig. S3A and S3B based on the plate theory are only indicative. Nevertheless, the predicted singularities of both radial and tangential strain are meaningful, suggesting the location where buckling may easily occur with rotational symmetry of order 6. This could be correlated to the experimental signature appeared in Figure 2 and 3.

From an engineering point of view, the design of the ABM with a three-level architecture (frame-nanofiber-BM) is the result of a trade-off of biomimicking and micro-processing. While the first level of the architecture (honeycomb frame) can be produced massively at low cost with various microfabrication techniques, the second level (monolayer of crosslinked nanofibers) can also be manufactured at low cost by electrospinning and the third level can be done by spraying a protein-containing solution to the device or dipping the device in a protein-containing solution. Since the geometry and size of the frame can be easily changed by design and other techniques (electrospinning, spraying, and dipping) can be explored with different material/molecules, the method proposed in this work is genetic which can be applied to a large variety of applications. For example, frames could be designed to generate a particular type of folding generally observed with an in vivo intestinal or skin epithelium. It could also be possible to pre-form the nanofiber backbone into dome- or tube-like shapes for replating hiPSC-derived or primary cells. Obviously, the fabricated ABM can be used to generate other types of epithelium, endothelium, or epithelium/endothelium co-culture systems, including intestinal barriers, brain blood barriers (BBB), etc. In this regard, it might be possible to develop an intestinal model to examine more closely the distribution of different cell types within a folded epithelium. In this regard, the ABM device might be an efficient alternative to hydrogel scaffolds [58] for future studies. Moreover, the generated cell layers can be easily integrated into a microfluidic device for organ-on-a-chip applications. Yet, a more comprehensive investigation has to be developed for both ABM characterization and real-time monitoring of the epilayer formation. More importantly, the functionality of generated alveolar epithelium has to be demonstrated, including the air-blood barrier formation, gas exchange, pathogen protection, etc. It is then important to develop real-time monitoring systems such as microfluidic TEER techniques for consistent data readout. Altogether, the method developed in this work hold potential for both basic research and advanced cell-based assays for toxicity testing, disease modelling, drug screening, tissue engineering, and regenerative medicine.

5. CONCLUSION

We described a method to develop alveolar epithelial cells on ABM. hiPSC-derived lung progenitors were used which led to remarkable epithelial deformation and folding without losing monolayered cell organization. The observed deformation patterns could be correlated to geometry-dependent strain distribution of the ABM and the epilayer. We also showed a high-level expression of SFTPC+ cells and an increase in AQP5+ cells with respect to that on a nanofiber-covered glass. Thus, our study demonstrates a type of self-organization of epithelial cells on BM-like culture support which allows cell-force generated tissue folding.

ACKNOWLEDGMENT

E.R. has been supported by Indonesia Endowment Fund for Education, Ministry of Finance of The Republic of Indonesia (LPDP). This work has been supported by grants from Agence Nationale pour la Recherche (ANR-17-CE09-0017, ANR-19-CE18-0009-01), Région Ile-de-France (DIM-ELICIT: AutoStemCell), PSL-valorization (program pre-maturation), Carnot IPGG, and European Commission Cost Action project BIONECA (CA 16122).

REFERENCES

[1] N. Štorgel, M. Krajnc, P. Mrak, J. Štrus, P. Ziherl, Quantitative Morphology of Epithelial Folds, Biophys. J. 110 (2016) 269–277. https://doi.org/10.1016/j.bpj.2015.11.024

[2] W. Xi, T.B. Saw, D. Delacour, C.T. Lim, B. Ladoux, Material approaches to active tissue mechanics, Nat. Rev. Mater. 4 (2019) 23–44. https://doi.org/10.1038/s41578-018-0066-z

[3] Andrew R. Harris, Loic Peter, Julien Bellis, Buzz Baum, Alexandre J. Kabla, and Guillaume T. Charras, Characterizing the mechanics of cultured cell monolayers, Proc. Natl. Acad. Sci. U. S. A. 109 (2012) 16449-16454. https://doi.org/10.1073/pnas.1213301109.

[4] L. A. Osório, E. Silva and R. E. Mackay, A Review of Biomaterials and Scaffold Fabrication for Organ-on-a-Chip (OOAC) Systems, Bioengineering 8 (2021) 113. https://doi.org/10.3390/bioengineering8080113

[5] R. Jayadev, D.R. Sherwood, Basement membranes. Curr Biol. 27 (2017) R207-R211. https://doi.org/10.1016/j.cub.2017.02.006

[6] N. Khalilgharibi and Y. Mao, To form and function: on the role of basement membrane mechanics in tissue development, homeostasis and disease Open Biol. 11 (2021) 200360. https://doi.org/10.1098/rsob.200360.

[7] Marchiando AM, Graham WV, Turner JR. Epithelial barriers in homeostasis and disease. Annu Rev Pathol. 5 (2010) 119-44. https://doi.org/10.1146/annurev.pathol.4.110807.092135.

[8] C.F. Guimarães, L. Gasperini, A.P. Marques, R.L. Reis, The stiffness of living tissues and its implications for tissue engineering, Nat. Rev. Mater. 5 (2020) 351–370. https://doi.org/10.1038/s41578-019-0169-1

[9] E. Hannezo, Cl-P Heisenberg, Mechanochemical Feedback Loops in Development and Disease, Cell 178 (2019) 12-25, https://doi.org/10.1016/j.cell.2019.05.052.

[10] Y. W. Chen, S. X. Huang, A. L. R. T. de Carvalho, S.-H. Ho, M. N. Islam, S. Volpi, L. D. Notarangelo, M. Ciancanelli, J. L. Casanova, J. Bhattacharya, A. F. Liang, L. M. Palermo, M. Porotto, A. Moscona, H. W. Snoeck, A three-dimensional model of human lung development and disease from pluripotent stem cells, Nature Cell Biology. 19 (2017) 542. https://doi.org/10.1038/ncb3510.

[11] S.K. Kim, Y.H. Kim, S. Park, S.W. Cho, Organoid engineering with microfluidics and biomaterials for liver, lung disease, and cancer modeling, Acta Biomater. 132 (2021) 37–51. https://doi.org/10.1016/j.actbio.2021.03.002.

[12] J. A. Whitsett, T. E. Weaver, Alveolar development and disease, Am J Respir Cell Mol Biol. 53 (2015) 1. https://doi.org/10.1165/rcmb.2015-0128PS.

[13] H.Ye, Q. Zhan, Y. Ren, X. Liu, C. Yang, C. Wang. Cyclic deformation-induced injury and differentiation of rat alveolar epithelial type II cells. Respir Physiol Neurobiol.180 (2012) 237-46.

https://doi.org/10.1016/j.resp.2011.11.011.

[14] M.I. Hermanns, R.E. Unger, K. Kehe, K. Peters, C.J. Kirkpatrick, Lung epithelial cell lines in coculture with human pulmonary microvascular endothelial cells: Development of an alveolo-capillary barrier in vitro, Lab. Investig. 84 (2004) 736–752. https://doi.org/10.1038/labinvest.3700081

[15] A. Costa, C. de Souza Carvalho-Wodarz, V. Seabra, B. Sarmento, C.M. Lehr, Triple co-culture of human alveolar epithelium, endothelium and macrophages for studying the interaction of nanocarriers with the air-blood barrier, Acta Biomater. 91 (2019) 235–247. https://doi.org/10.1016/j.actbio.2019.04.037.

[16] K. Hurley, J. Ding, C. Villacorta-Martin, M.J. Herriges, A. Jacob, M. Vedaie, K.D. Alysandratos, Y.L. Sun, C. Lin, R.B. Werder, J. Huang, A.A. Wilson, A. Mithal, G. Mostoslavsky, I. Oglesby, I.S. Caballero, S.H. Guttentag, F. Ahangari, N. Kaminski, A. Rodriguez-Fraticelli, F. Camargo, Z. Bar-Joseph, D.N. Kotton, Reconstructed Single-Cell Fate Trajectories Define Lineage Plasticity Windows during Differentiation of Human PSC-Derived Distal Lung Progenitors, Cell Stem Cell. 26 (2020) 593-608.e8. https://doi.org/10.1016/j.stem.2019.12.009.

[17] K.M. Abo, L. Ma, T. Matte, J. Huang, K. D. Alysandratos, R. B. Werder, A. Mithal, M.L. Beermann, J. Lindstrom-Vautrin, G. Mostoslavsky, L. Ikonomou, D. N. Kotton, F. Hawkins, A. Wilson, and C. Villacorta-Martin, Human iPSC-derived alveolar and airway epithelial cells can be cultured at air-liquid interface and express SARS-CoV-2 host factors, BioRxiV. (2020) https://doi.org/10.1101/2020.06.03.132639.

[18] D.N.K. J. Huang, A. J. Hume, K. M. Abo, R. B. Werder, C. Villacorta-Martin, K-D. Alysandratos, M. L. Beermann, C. Simone-Roach, J. Lindstrom-Vautrin, J. Olejnik, E. L. Suder, E. Bullitt, A. Hinds, A. Sharma, M. Bosmann, R. Wang, F. Hawwkins, E. J. Burks, M. Saee, SARS-CoV-2 Infection of pluripotent stem cell-derived human lung alveolar type 2 cells elicits a rapid epithelial-intrinsic inflammatory response, BioRxiV. (2020) https://doi.org/10.1101/2020.06.30.175695

[19] M. Trevisan, S. Riccetti, A. Sinigaglia, L. Barzon, Sars-cov-2 infection and disease modelling using stem cell technology and organoids, Int. J. Mol. Sci. 22 (2021) 1–19. https://doi.org/10.3390/ijms22052356

[20] M. Ghaedi, E.A. Calle, J.J. Mendez, A.L. Gard, J. Balestrini, A. Booth, P.F. Bove, L. Gui, E.S. White, L.E. Niklason, Human iPS cell-derived alveolar epithelium repopulates lung extracellular matrix, J. Clin. Invest. 123 (2013) 4950–4962. https://doi.org/10.1172/JCI68793

[21] S.X.L. Huang, M.N. Islam, J. O'Neill, Z. Hu, Y.G. Yang, Y.W. Chen, M. Mumau, M.D. Green, G. Vunjak-Novakovic, J. Bhattacharya, H.W. Snoeck, Efficient generation of lung and airway epithelial cells from human pluripotent stem cells, Nat. Biotechnol. 32 (2014) 84–91. https://doi.org/10.1038/nbt.2754

[22] H.R. Heo, J. Kim, W.J. Kim, S.R. Yang, S.S. Han, S.J. Lee, Y. Hong, S.H. Hong, Human pluripotent stem cell-derived alveolar epithelial cells are alternatives for in vitro pulmotoxicity assessment, Sci.

Rep. 9 (2019) 1–11. https://doi.org/10.1038/s41598-018-37193-3

[23] Y. He, E. Rofaani, X. Huang, B. Huang, F. Liang, L. Wang, J. Shi, J.Peng, Y. Chen, Efficient generation of alveolar epithelium using reconstituted basement membrane and hiPSC-derived organoids, Adv Heal. Mat. (2022) 2101972. https://doi.org/10.1002/adhm.202101972

[24] D. Huh, B.D. Matthews, A. Mammoto, M. Montoya-Zavala, H. Yuan Hsin, D.E. Ingber, Reconstituting organ-level lung functions on a chip, Science 80 (2010) 1662–1668. https://doi.org/10.1126/science.1188302

[25] A.O. Stucki, J.D. Stucki, S.R.R. Hall, M. Felder, Y. Mermoud, R.A. Schmid, T. Geiser, O.T. Guenat, A lung-on-a-chip array with an integrated bio-inspired respiration mechanism, Lab Chip. 15 (2015) 1302–1310. https://doi.org/10.1039/C4LC01252F

[26] E. Rofaani, J. Peng, L. Wang, Y. He, B. Huang, Y. Chen, Fabrication of ultrathin artificial basement membrane for epithelial cell culture, Microelectron. Eng. 232 (2020) 111407. https://doi.org/10.1016/j.mee.2020.111407

[27] Y. Zhang, Large deflection of clamped circular plate and accuracy of its approximate analytical solutions. Science China Physics, Mechanics & Astronomy, 59 (2016) 624602. https://doi.org/10.1007/s11433-015-5751-y

[28] E. Rofaani, B. Huang, J. Peng, Y. Chen, Reconstituted basement membrane enables airway epithelium modelling and nanoparticle toxicity testing, Int. J. of Biological Macromolecule. 204 (2022) 300. https://doi.org/10.1016/j.ijbiomac.2022.02.018

[29] M. Radiom, Y. He, J. Peng-Wang, A. Baeza-Squiban, J.-F. Berret, Y. Chen, Alveolar mimics with periodic strain and its effect on the cell layer formation, Biotechnology and Bioengineering. 117 (2020) 2827. https://doi.org/10.1002/bit.27458.

[30] B.X. Huang, J. Peng, X.C. Huang, F. Liang, L. Wang, J. Shi, A. Yamada and Y. Chen, Generation of Interconnected Neural Clusters in Multiscale Scaffolds from Human-Induced Pluripotent Stem Cells, ACS Appl. Mater. Interfaces 13 (2021) 55939–55952. https://doi.org/10.1021/acsami.1c18465.

[31] F. Hawkins, D.N. Kotton, Embryonic and induced pluripotent stem cells for lung regeneration, Ann. Am. Thorac. Soc., 12, Suppl 1 (2015) S50–S53. https://doi.org/ 10.1513/AnnalsATS.201410-457MG

[32] A. Hartsock, W.J. Nelson, Adherens and tight junctions: Structure, function and connections to the actin cytoskeleton, Biochim. Biophys. Acta - Biomembr. 1778 (2008) 660–669. https://doi.org/10.1016/j.bbamem.2007.07.012

[33] K. D. Sumigray, M. Terwilliger, T. Lechler, Morphogenesis and Compartmentalization of the Intestinal Crypt, Developmental Cell,45 (2018) 183-197.e5, https://doi.org/10.1016/j.devcel.2018.03.024

[34] L. N. Frank, The pulmonary alveolar epithelium of laboratory mammals and man, 117 (1953) 241–

263. https://doi.org/ 10.1002/ar.1091170208

[35] F. Chen, A. Fine, Stem Cells in Lung Injury and Repair, Am. J. Pathol. 186 (2016) 2544–2550. https://doi.org/ 10.1016/j.ajpath.2016.05.023

[36] D. Marcetic, M. Samaržija, A. V. Dugac, J. Kneževic, Angiotensin-Converting Enzyme 2 (ACE2) as a Potential Diagnostic and Prognostic Biomarker for Chronic Inflammatory Lung Diseases, Genes 12 (2021) 1054. https://doi.org/10.3390/genes12071054.

[37] A.K Yip, P. Huang, K.H. Chiam, Cell-Cell Adhesion and Cortical Actin Bending Govern Cell Elongation on Negatively Curved Substrates. Biophys J. 114 (2018) 1707-1717. https://doi.org/10.1016/j.bpj.2018.02.027

[38] E. Latorre, S. Kale, L. Casares, Active superelasticity in three-dimensional epithelia of controlled shape. Nature 563 (2018) 203–208. https://doi.org/10.1038/s41586-018-0671-4

[39] T.P.J.Wyatt, J. Fouchard, A. Lisica, N. Khalilgharibi, B. Baum, P. Recho, A. J.Kabla, G.T. Charras, Actomyosin controls planarity and folding of epithelia in response to compression. Nat. Mater. 19 (2020) 109–117. https://doi.org/10.1038/s41563-019-0461-x

[40] L. Liu, M. Yoshioka, M. Nakajima, A. Ogasawara, J. Liu, K. Hasegawa, S. Li, J. Zou, N. Nakatsuji, K.-i. Kamei, Nanofibrous gelatin substrates for long-term expansion of human pluripotent stem cells, Biomaterials 35(24) (2014) 6259-6267.

[41] Y. Tang, L. Liu, J. Li, L. Yu, L. Wang, J. Shi, Y. Chen, Induction and differentiation of human induced pluripotent stem cells into functional cardiomyocytes on a compartmented monolayer of gelatin nanofibers, Nanoscale. 8 (2016) 14530–14540. https://doi.org/10.1039/c6nr04545f.

[42] Y. Tang, L. Liu, J. Li, L. Yu, F.P.U. Severino, L. Wang, J. Shi, X. Tu, V. Torre, Y. Chen, Effective motor neuron differentiation of hiPSCs on a patch made of crosslinked monolayer gelatin nanofibers, J. Mater. Chem. B. 4 (2016) 3305–3312. https://doi.org/10.1039/c6tb00351f.

[43] Y. Tang, F. P. Ulloa Severino, F. Iseppon, V. Torre, Y. Chen, Patch method for culture of primary hippocampal neurons, Microelectronic Engineering. 175 (2017) 61. https://doi.org/10.1016/j.mee.2017.01.012

[44] S. Li, M. Yoshioka, J. Li, L. Liu, S. Ye, K.I. Kamei, Y. Chen, Nanocasting of fibrous morphology on a substrate for long-term propagation of human induced pluripotent stem cells. Biomed Mater. (2022) https://doi.org/10.1088/1748-605X/ac51b8

[45] J.L. Gibson, M.F. Ashby, Cellular Solids: Structure and Properties, 2nd ed, Cambridge Univ. Press. (1997). https://doi.org/10.1017/CBO9781139878326

[46] J. Huynh, Joseph P. Califano, and Cynthia A. Reinhart-King, Chapter 4: Cell-Generated Forces in Tissue Assembly, Function, and Disease, in “Mechanobiology of Cell-Cell and Cell-Matrix Interactions”, A. Wagoner Johnson and Brendan A.C. Harley (Eds) Springer, Boston, MA (2011). ISBN: 978-1-4419-8083-0.

[47] H. Ogita, Yoshimi Takai, Cross-talk among integrin, cadherin, and growth factor receptor: roles of nectin and nectin-like molecule, Int. Rev Cytol. 265 (2008) 1–54. https://doi.org/10.1016/S0074-7696(07)65001-3.

[48] M.A. Schwartz, D.W. DeSimone, Cell adhesion receptors in mechanotransduction, Curr. Opin. Cell Biol. 20 (2008) 551–556. https://doi.org/ 10.1016/j.ceb.2008.05.005

[49] J. Chlasta, P. Milani, G. Runel, J.L. Duteyrat, L. Arias, L.A. Lamiré, A. Boudaoud, M. Grammont, Variations in basement membrane mechanics are linked to epithelial morphogenesis, Dev. 144 (2017) 4350–4362. https://doi.org/10.1242/dev.152652.

[50] C.M. Nelson, R.P. Jean, J.L. Tan, W.F. Liu, N.J. Sniadecki, A.A. Spector, C.S. Chen, Emergent patterns of growth controlled by multicellular form and mechanics, Proc. Natl. Acad. Sci. U. S. A. 102 (2005) 11594–11599. https://doi.org/10.1073/pnas.0502575102.

[51] C. Rauskolb, S. Sun, G. Sun, Y. Pan, K.D. Irvine, Cytoskeletal tension inhibits Hippo signaling through an Ajuba-Warts complex, Cell. 158 (2014) 143–156. https://doi.org/10.1016/j.cell.2014.05.035

[52] E. Hannezo, J. Prost, and J.-F. Joanny, Instabilities of Monolayered Epithelia: Shape and Structure of Villi and Crypts, Phys. Rev. Lett. 107 (2011) 078104, https://doi.org/10.1103/PhysRevLett.107.078104

[53] H. Koyama, D. Shi, T. Fujimori, Biophysics in oviduct: Planar cell polarity, cilia, epithelial fold and tube morphogenesis, egg dynamics, Biophys. Physicobiology. 16 (2019) 89–107. https://doi.org/10.2142/biophysico.16.0_89.

[54] M. Tozluoğlu, M. Duda, N.J. Kirkland, R. Barrientos, J.J. Burden, J.J. Muñoz, Y. Mao, Planar Differential Growth Rates Initiate Precise Fold Positions in Complex Epithelia, Dev. Cell. 51 (2019) 299-312.e4. https://doi.org/10.1016/j.devcel.2019.09.009.

[55] T.B. Saw, A. Doostmohammadi, V. Nier, L. Kocgozlu, S. Thampi, Y. Toyama, P. Marcq, C.T. Lim, J.M. Yeomans, B. Ladoux, Topological defects in epithelia govern cell death and extrusion, Nature. 544 (2017) 212–216. https://doi.org/10.1038/nature21718.

[56] E.J. Pearl, J. Li, J.B.A. Green, Cellular systems for epithelial invagination, Philos. Trans. R. Soc. B Biol. Sci. 372 (2017) 0–3. https://doi.org/10.1098/rstb.2015.0526.

[57] E. Hannezo, J. Prost, J-F. Joanny, Instabilities of monolayered epithelia: shape and structure of villi and crypts, Phys Rev Lett 107 (2011) 078104, https://doi.org/10.1103/PhysRevLett.107.078104.

[58] W. Xi, J. Saleh, A. Yamada, C. Tomba, B. Mercier, S. Janel, T. Dang, M. Soleilhac, A. Djemat, H. Wu, B. Romagnolo, F. Lafont, R. Mège, Y. Chen, D. Delacour, Modulation of designer biomimetic matrices for optimized differentiated intestinal epithelial cultures,Biomaterials, 282 (2022) 121380, https://doi.org/10.1016/j.biomaterials.2022.121380.

Figure caption

Figure 1 Artificial basement membrane (ABM) and alveolar epithelial formation. (A) Scanning electron microscopy images of monolayer of crosslinked nanofibers and ABM after self-assembling of collagen IV and laminin. (B) Stepwise differentiation of human induced stem cells to alveolar cells. (C) Schematic diagram of involved culture conditions.

Figure 2 Confocal fluorescence images of hiPSC-derived alveolar progenitor cells on ABM Cells were stained by NKX2.1 (green), ZO-1 (red), and DAPI (blue) 6 days after plating. (A) Section views of epithelial folding from the top (56 μm) to bottom (2 μm). (B) Top view of 3D construction of the cell layer after ZO-1 staining. (C) Cross-sectional views of different XZ planes. (D) Cross-sectional views of an XZ plan, showing expression levels of alveolar progenitor specific proteins. Scale bars: 50 μm.

Figure 3 Comparison of hiPSC-derived alveolar progenitor cells on different substrates. Cells were stained by NKX2.1 (green), ZO-1 (red), and DAPI (blue) 6 days after plating on glass, nanofiber substrate (NFS), and ABM. (A) Immunofluorescence images showing monolayer organizations with two types of singularities (yellow circle marked). Scale bars: 20 μm. (B) Schematic illustration of typical epithelial singularities. (C) Statistics of cell density, NKX2.1, and ZO-1 expression levels of the cells on different types of substrates.

Figure 4 Immunofluorescence images of matured alveolar epithelial cells on ABM. Cells were stained by SFTPC (green), AQP5 (red), and DAPI (blue) 17 days after plating. (A) Projection view of a Z-stack of microscope images. (B) Cross-sectional views of four XZ plane indicated in (A). (C) Selected sectional views from the Z-stack. Scale bars: 50 μm.

Figure 5 Immunofluorescence images of matured alveolar epithelial cells. Cells were stained by SFTPC (green), AQP5 (red), and DAPI (blue) 17 days after plating on NFS and ABM. (A) Cross-sectional views at XY and XZ planes. (B) Zoom view at AZ plane. (C) Zoom

views at the top and bottom XY planes. Statistical analyses of (D) cell density per 100x100 μm², (E) cell height, (F, G) fluorescence intensity of Z-stack projection for SFTPC and AQP5, respectively. (H) Percentage of SFTPC+; SFTPC+/AQP5+; and AQP5+ cells. Scale bars: 50 μm.

Figure 6 Immunofluorescence images of matured alveolar epithelial cells. Cell were stained with ACE2 (green) and TMPRSS2 (red) antibodies and DAPI (blue) 17 days after plating on NFS and ABM. (A) Comparison of the ACE2 distribution. White and yellow arrows indicate dispersed and clustered-ACE2 expression, referred as ABM-D and ABM-C, respectively. (B) Percentage of ACE2+ cells. (C) ACE2 expression levels of the cells. (D) Distribution of TMPRSS and ACE2 proteins. Scale bar is 50 μm.

Figure 1

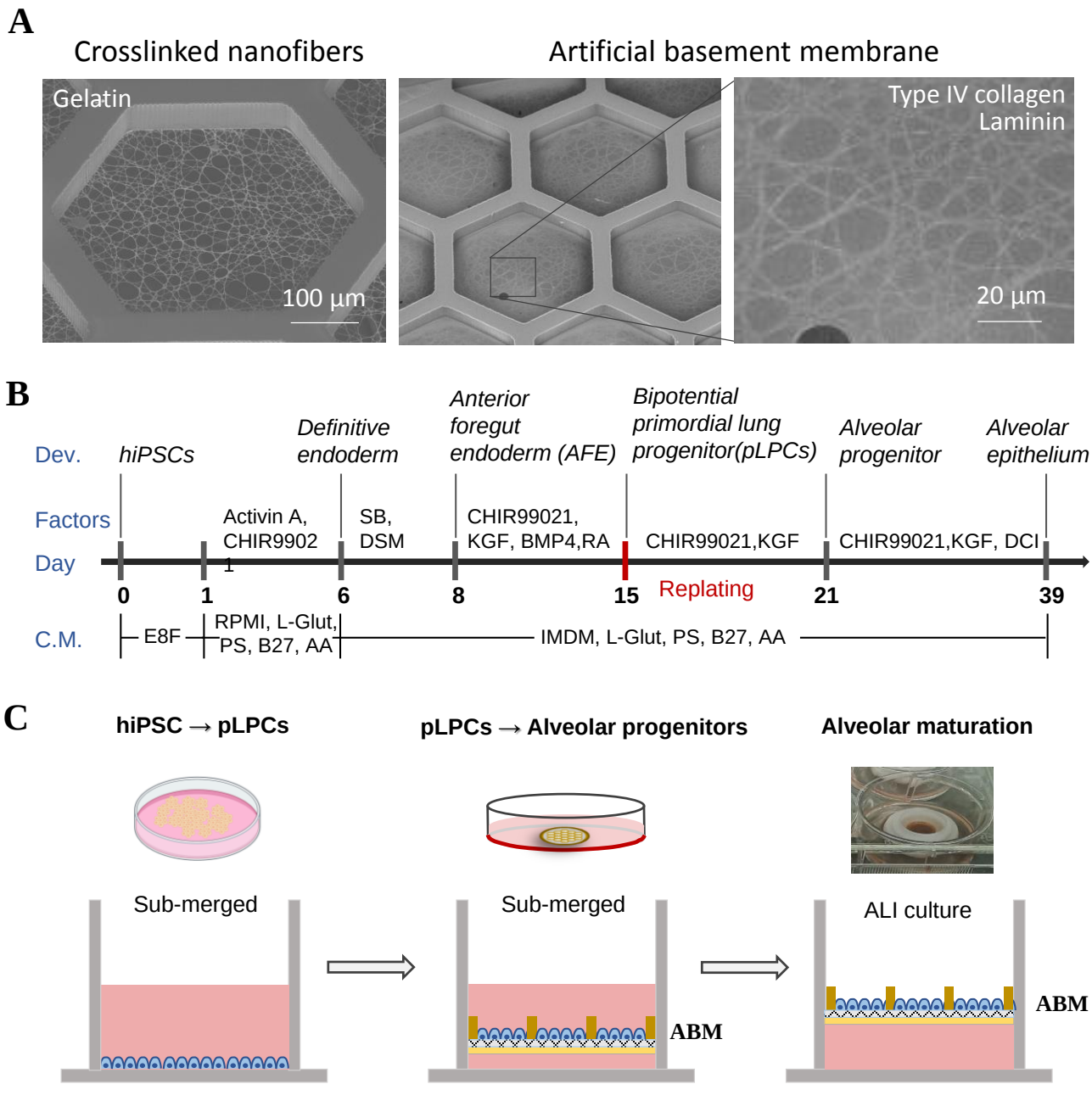
A
Crosslinked nanofibers
Artificial basement membrane
Gelatin
100 μm
Type IV collagen
Laminin
20 μm
B
Dev.
hiPSCs
Definitive endoderm
Anterior foregut endoderm (AFE)
Bipotential primordial lung progenitor(pLPCs)
Alveolar progenitor
Alveolar epithelium
Factors
Activin A, CHIR99021
SB, DSM
CHIR99021, KGF, BMP4,RA
CHIR99021,KGF
CHIR99021,KGF, DCI
Day
0
1
6
8
15
Replating
21
39
C.M.
E8F
RPMI, L-Glut, PS, B27, AA
IMDM, L-Glut, PS, B27, AA
C
hiPSC → pLPCs
pLPCs → Alveolar progenitors
Alveolar maturation
Sub-merged
Sub-merged
ALI culture
ABM
ABM

Figure 2

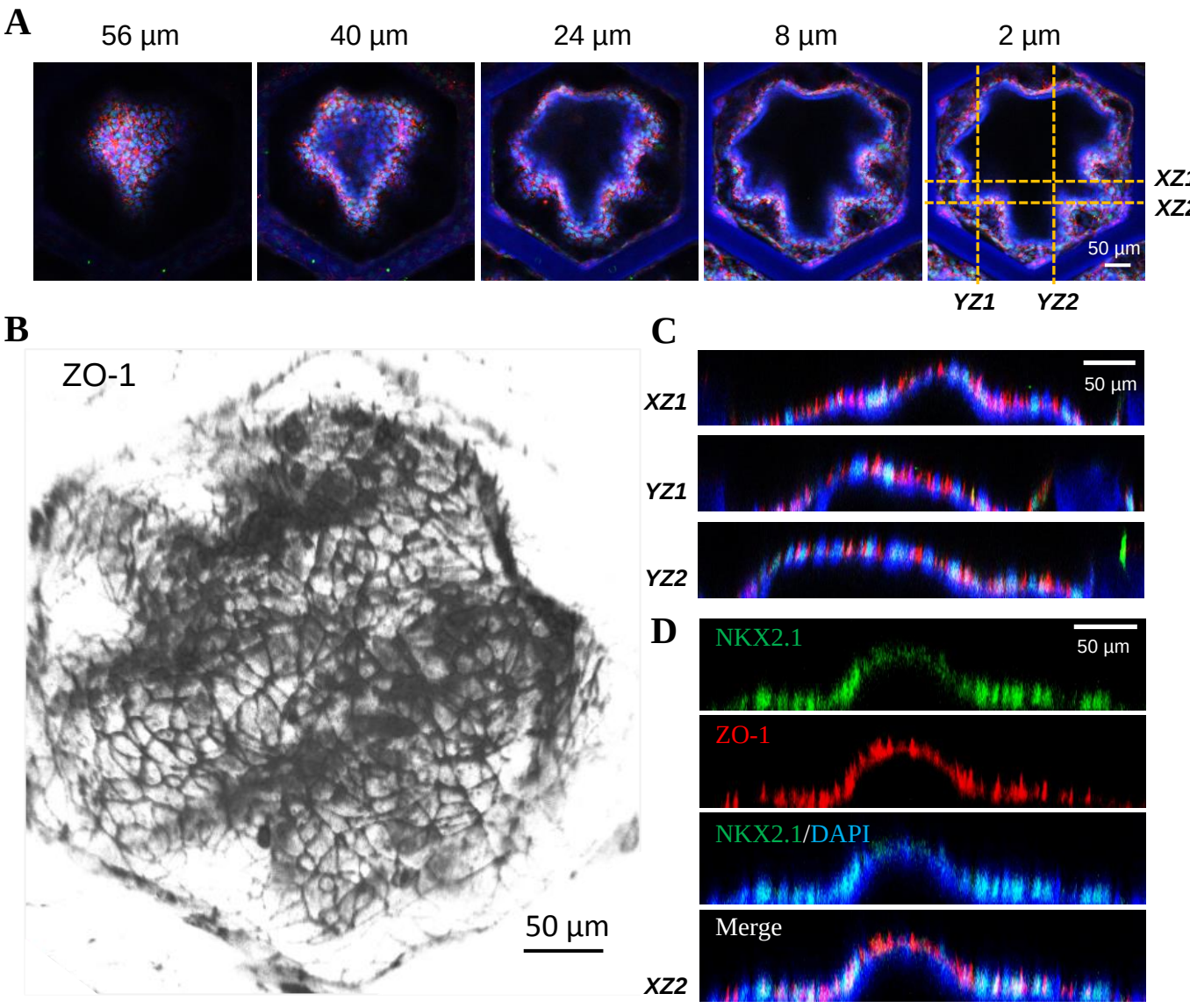
A
56 µm
40 µm
24 µm
8 µm
2 µm
50 µm
YZ1
YZ2
B
ZO-1
50 µm
C
XZ1
YZ1
YZ2
50 µm
D
NKX2.1
50 µm
ZO-1
NKX2.1/DAPI
Merge
XZ2

Figure 3

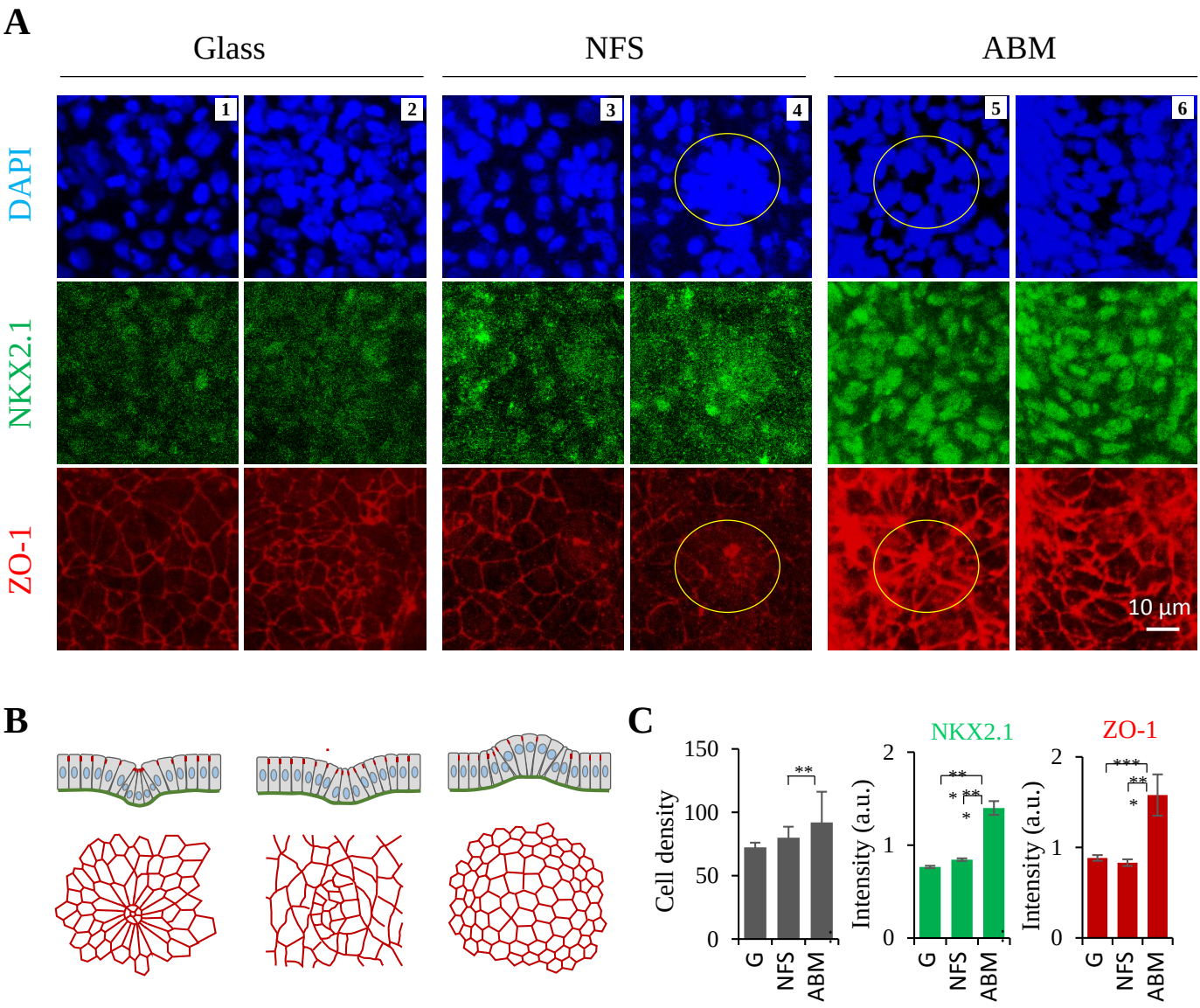
A
Glass
NFS
ABM
DAPI
NKX2.1
ZO-1
1
2
3
4
5
6
10 µm
B
C
NKX2.1
ZO-1
Cell density
Intensity (a.u.)
Intensity (a.u.)
150
100
50
0
2
1
0
G
NFS
ABM
**
**
*
**
*
***
**
*

Figure 4

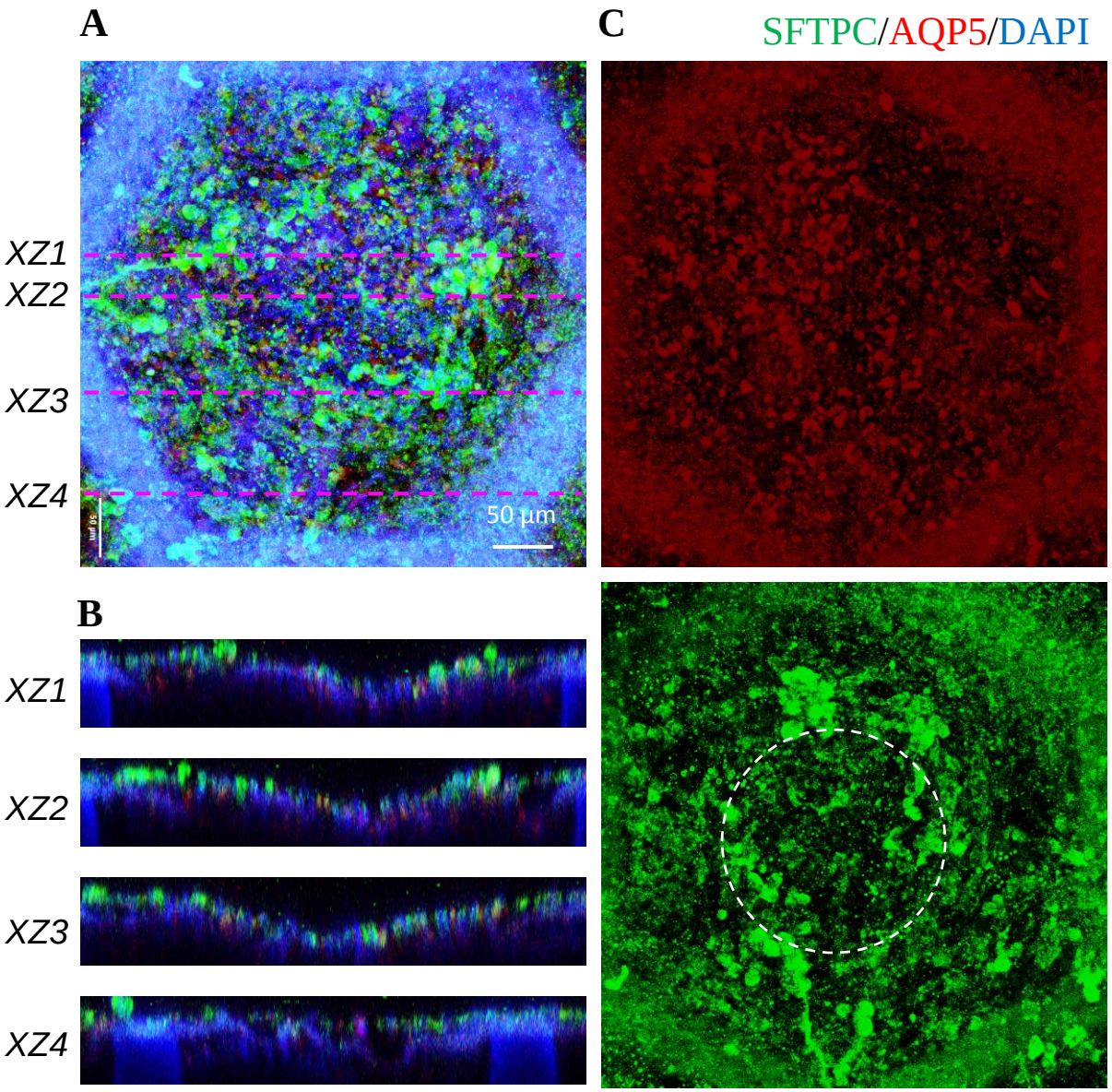

Figure 5

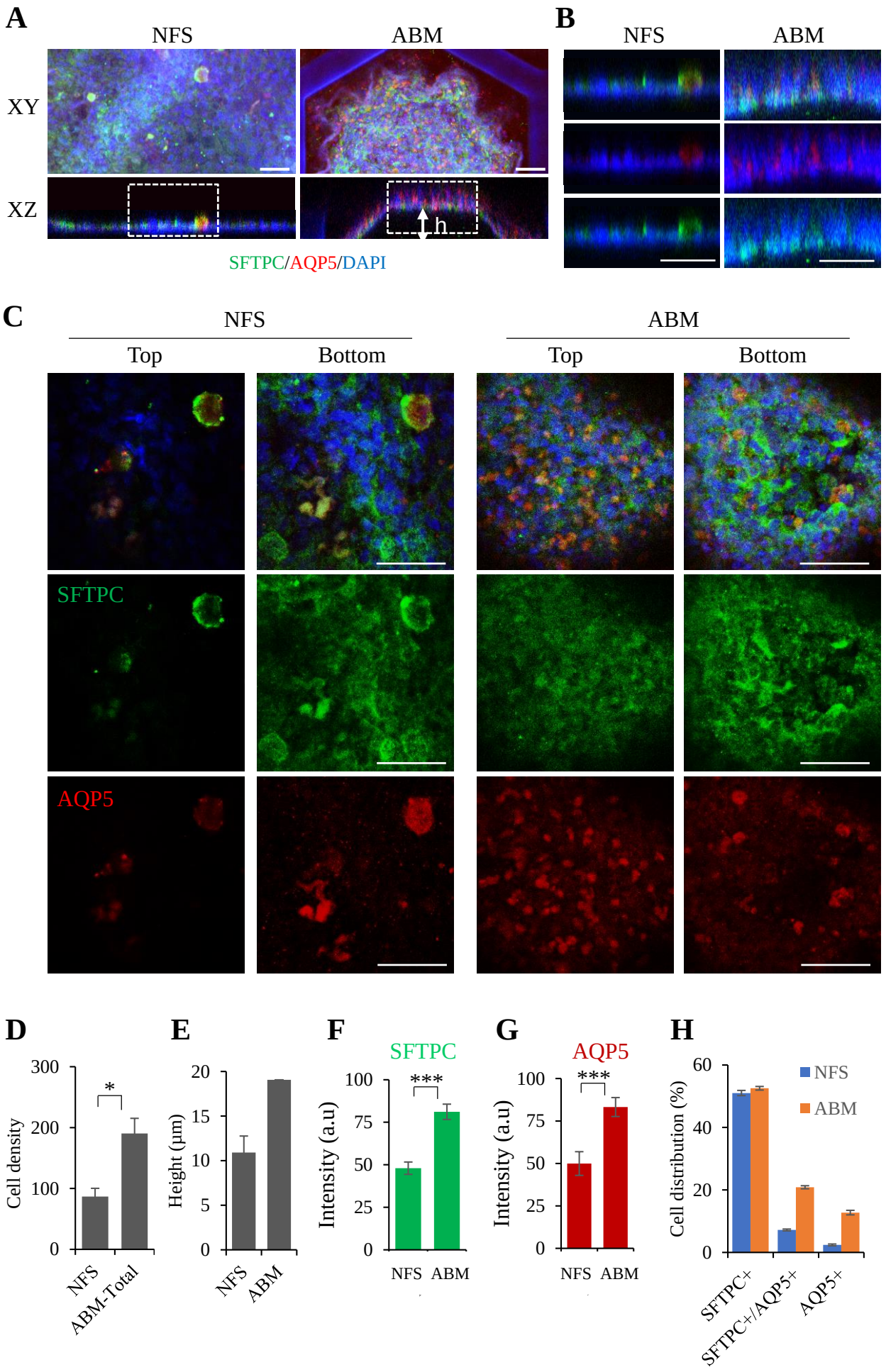
A
NFS
ABM
XY
XZ
h
SFTPC/AQP5/DAPI
B
NFS
ABM
C
NFS
ABM
Top
Bottom
Top
Bottom
SFTPC
AQP5
D
Cell density
300
200
100
0
*
NFS
ABM-Total
E
Height (μm)
20
15
10
5
0
NFS
ABM
F
SFTPC
Intensity (a.u)
100
75
50
25
0
***
NFS
ABM
G
AQP5
Intensity (a.u)
100
75
50
25
0
***
NFS
ABM
H
Cell distribution (%)
60
40
20
0
NFS
ABM
SFTPC+
SFTPC+/AQP5+
AQP5+

Figure 6

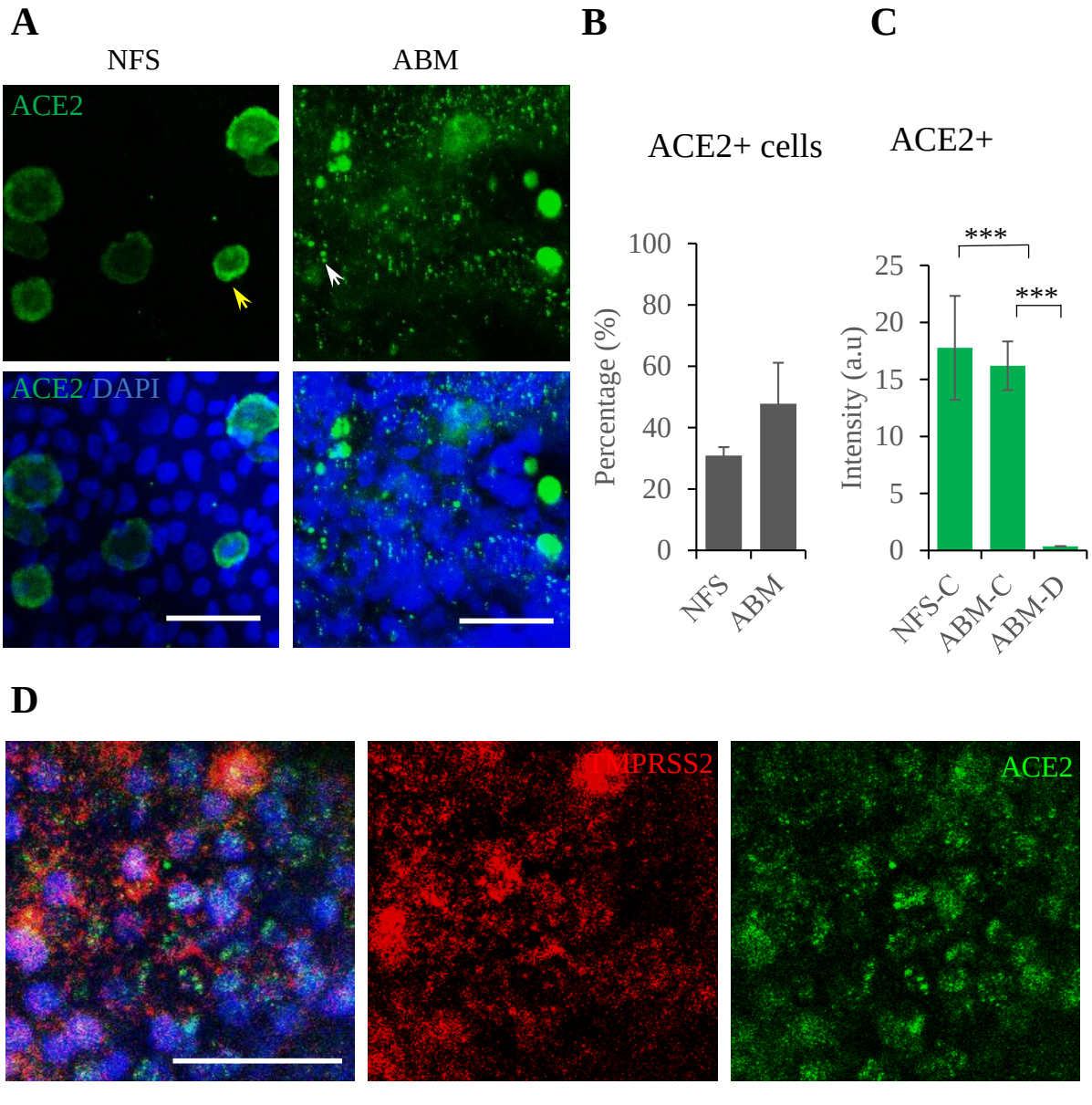
A
NFS
ABM
ACE2
ACE2/DAPI
B
ACE2+ cells
Percentage (%)
100
80
60
40
20
0
NFS
ABM
C
ACE2+
Intensity (a.u)
25
20
15
10
5
0
***
***
NFS-C
ABM-C
ABM-D
D
TMPRSS2
ACE2

Figure S1

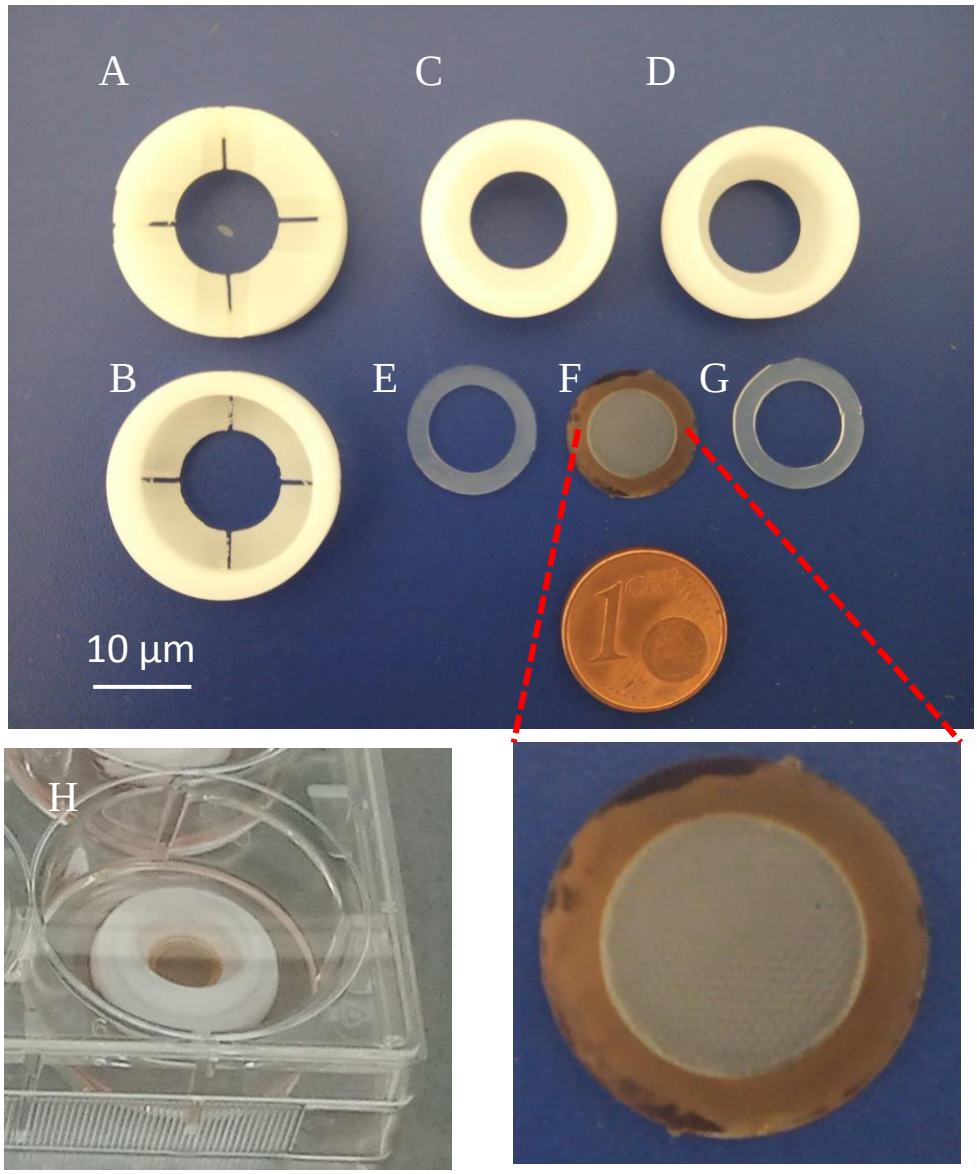

A: Basal part (bottom view)
B: Basal part (top view)
C: Apical part (bottom view)
D: Apical part (top view)
E: PDMS ring (for basal part)
F: ABM
G: PDMS ring (for apical part)
H: Assembly in a 6 well plate

Fig. S2

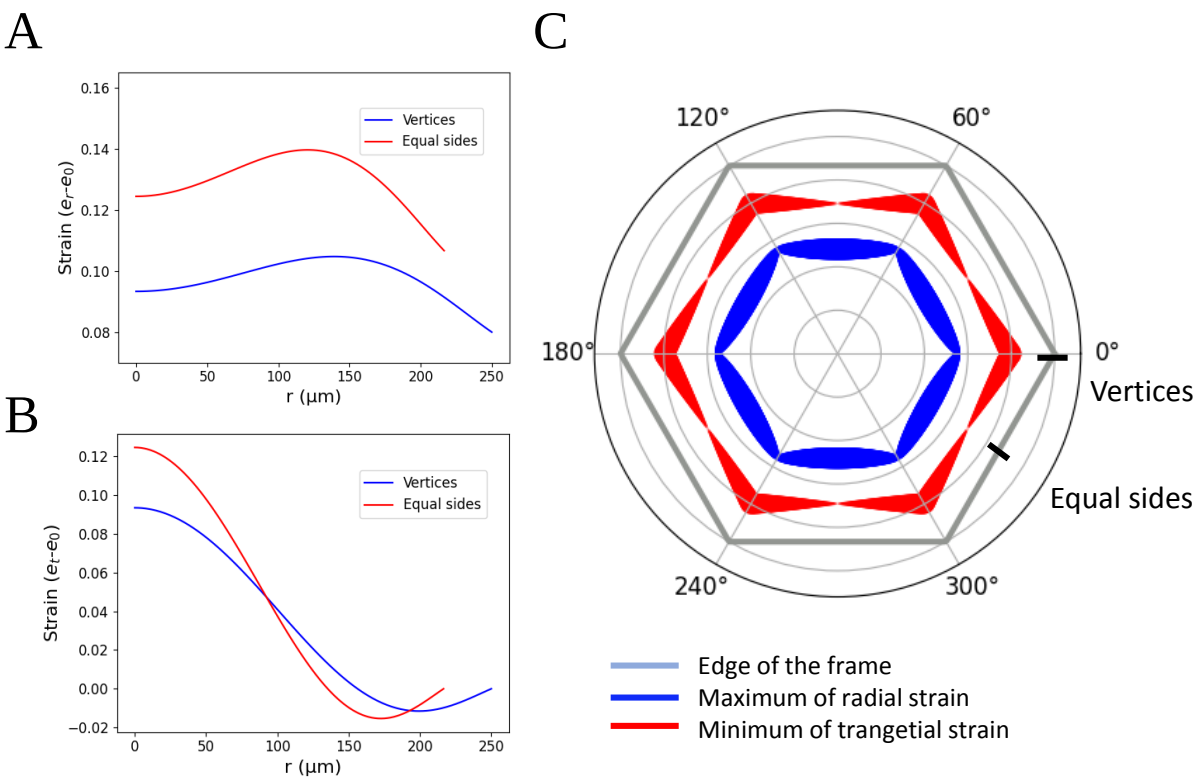
A
B
C
Vertices
Equal sides
Strain (e_r-e_0)
Strain (e_t-e_0)
r (μm)
120°
60°
180°
0°
240°
300°
Vertices
Equal sides
Edge of the frame
Maximum of radial strain
Minimum of trangetial strain

Fig. S3

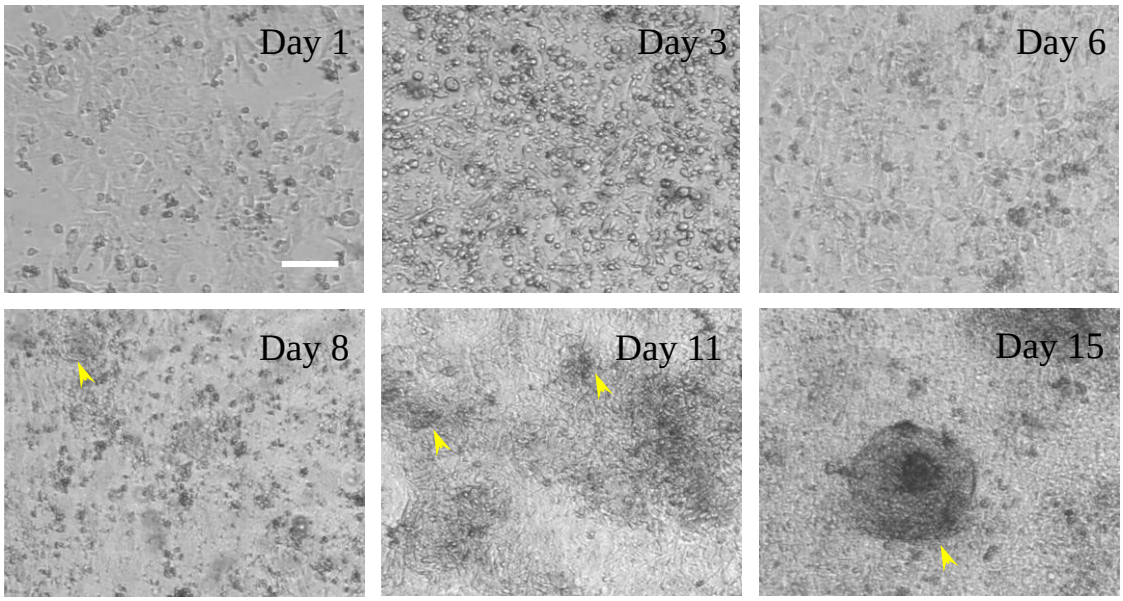

Fig. S4